





# First Demonstration of Dynamic High-Gain Beam Steering With a Scanning Lens Phased Array

**SJOERD BOSMA** <sup>1</sup> (Graduate Student Member, IEEE), **NICK VAN ROOIJEN** <sup>1</sup>,  
**MARIA ALONSO-DELPINO** <sup>1</sup> (Senior Member, IEEE), **MARCO SPIRITO**<sup>2</sup> (Member, IEEE),  
**AND NURIA LLOMBART** <sup>1</sup> (Fellow, IEEE)

(Regular Paper)

<sup>1</sup>Terahertz Sensing Group, Department of Microelectronics, Delft University of Technology, 2628 CD Delft, The Netherlands

<sup>2</sup>Electronics Research Laboratory, Department of Microelectronics, Delft University of Technology, 2628 CD Delft, The Netherlands

CORRESPONDING AUTHOR: Sjoerd Bosma (e-mail: s.bosma@tudelft.nl).

This work was supported by the European Research Council under Starting Grant LAA-THz-CC-639749.

---

**ABSTRACT** We report on the first demonstration of dynamic beam steering using a scanning lens phased array. A scanning lens phased array relies on a combination of mechanical and electrical phase shifting to dynamically steer a high-gain beam beyond the grating-lobe free region using a sparse array. These two concepts have been demonstrated separately in the past, here we present, for the first time, a prototype demonstration where active mechanical and electrical phase shifting are combined. For this purpose, we have developed a sparse 4x1 scanning lens phased array at W-band (75-110 GHz) capable of beam steering a directive beam (>30 dBi) towards  $\pm 20^\circ$  with low grating lobe levels (around -10 dB). The lens array is fed by a waveguide-based leaky-wave feeding architecture that illuminates the lenses with high aperture efficiency over a wide bandwidth, which is required in the proposed scanning lens phased array architecture. The electrical phase shifting has been implemented using IQ-mixers around 15 GHz in combination with x6 multipliers to reach the W-band. The mechanical phase shifting relies on a piezo-electric motor, which is able to achieve displacements of the lens array of 6 mm with an accuracy of a few nanometers. The entire active array is calibrated over the air with an ad-hoc quasi-optical measurement setup. Resulting measurements show excellent agreement with the anticipated performance.

**INDEX TERMS** Beam steering, lens antennas, millimeter waves, phase shifting, phased arrays.

---

## I. INTRODUCTION

Millimeter- and submillimeter-wave scanning arrays will play a major role in communication and sensing scenarios in future 6G networks and automotive applications [1], [2]. Antennas for such applications should achieve very high gains (>30 dBi) and include dynamic scanning capabilities [3], [4]. Fully sampled phased arrays at or above 100 GHz, such as [5]–[10], are capable of wide-angle beam scanning but have low gain due to the limited number of array elements. Increasing the number of elements in such arrays is difficult due to thermal and integration constraints.

To overcome these limitations, we have recently proposed a scanning lens phased array concept in [11] that achieves a

high-gain, steerable beam using a very sparse array of only a few electrically large lens antenna elements. The geometry of the scanning lens phased array is indicated in Fig. 1(a). The grating lobes resulting from the sparsity of the array are suppressed by the directive beams from the lens elements. To achieve this suppression, high aperture efficiency lens antennas are required as the array elements [11].

Beam steering beyond the grating-lobe-free region from this sparse lens array is achieved by mechanically displacing the lens array relative to their feeds and, simultaneously, applying a relative electronic phase shift between the array elements. The mechanical displacement causes the element pattern of the lenses to be steered towards the desired

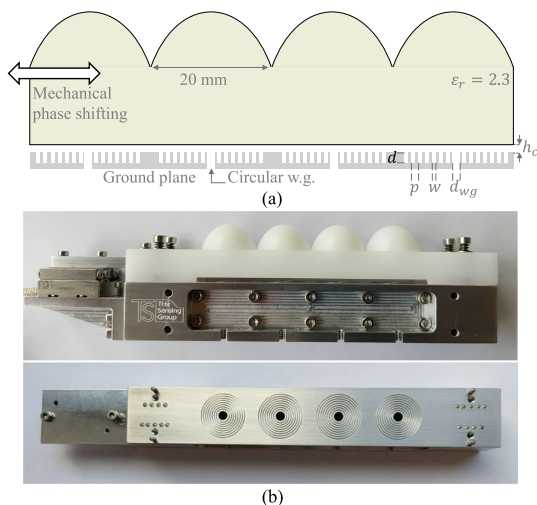


**FIGURE 1.** (a) Geometry of the 4x1 W-band scanning lens phased array. The ground plane contains periodic annular corrugations. (b) Photographs of the assembled prototype (top) including the piezo-motor and of the corrugated ground plane (bottom).

angle, while the electronic phase shifts steer the array factor. The steering of the element pattern enables achieving low grating lobe levels when scanning beyond the grating-lobe-free region, in contrast to limited scan arrays [12]–[16]. The required mechanical displacement for such lens arrays can be achieved by using a piezo-electric motor, as demonstrated in [11], [17]. Static phase shifting of these kinds of arrays has been demonstrated at 10 GHz [18] and 30 GHz in [4] by using corporate feeding networks. In [19], the contributions of each lens antenna at 38 GHz were measured independently and subsequently delayed by the required phase shift in post-processing before being summed. Thus, the combination of mechanical displacement and active electronic phase shifting to realize dynamic steering has not yet been demonstrated.

In this paper, we demonstrate a 4x1 W-band (75–110 GHz) scanning lens phased array prototype using the combination of a piezo-electric motor and an electronic phase steering architecture based on low frequency IQ-mixers and multipliers [20]. The design, simulated performance and fabrication of the lens array prototype is described in Section II. The embedded lens elements are characterized in Section III. We present the active array demonstration setup in Section IV, the over-the-air calibration setup in Section V and the demonstration of the active array in Section VI. Conclusions are drawn in Section VII.

## II. LENS ARRAY PROTOTYPE AT W-BAND

We have designed a 4x1 lens phased array with a periodicity of 20 mm ( $6\lambda_0$ ) at W-band ( $\lambda_0$  being the free-space wavelength at 90 GHz), which achieves a gain larger than 30 dBi. The design, simulated performance and fabrication of the array prototype are detailed in this section.

### A. SINGLE LENS ANTENNA DESIGN

In order to control the level of the grating lobes, the single lens antenna must be illuminated with high aperture efficiency

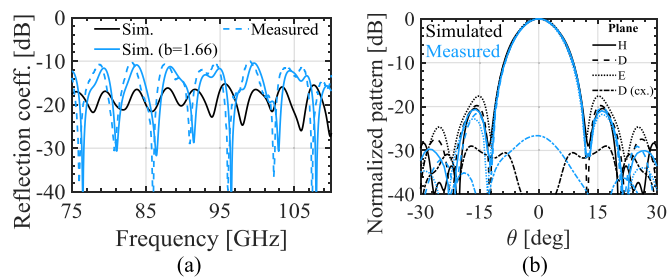


**FIGURE 2.** (a) Reflection coefficient of a single lens element as simulated (solid) and measured (dashed). Note that due to a fabrication error, a waveguide with  $b = 1.66$  mm was fabricated. (b) Single lens element radiation pattern simulated (black) and measured (blue) at 90 GHz.

as explained in [11]. To achieve this high efficiency over a wide bandwidth, we use the leaky-wave lens feed proposed in [21] and shown in Fig. 1(a). This feed consists of a circular waveguide with a diameter of  $d_{wg} = 3.18$  mm in a ground plane with annular corrugations, a half-wavelength air cavity and a high-density polyethylene (HDPE) elliptical lens with  $\epsilon_r = 2.3$ . The air cavity with height  $h_c = \lambda_0/2$  supports three leaky-wave modes of which only the main  $TE_1/TM_1$  modes contribute to broadside radiation [22]. The spurious  $TM_0$  mode is suppressed over a 2:1 bandwidth by the annular corrugations, as demonstrated in [21]. The dimensions of the corrugations and the diameter of the circular waveguide in this design are derived from [21] to the W-band and have a periodicity of  $p = 0.75$  mm, a width of  $w = 0.35$  mm and a depth of  $d = 1.1$  mm. The lens geometry is then derived in closed form based on the leaky-wave propagation constants using the procedure in [23]. We evaluated the aperture efficiency of this lens antenna using the Fourier Optics (FO) methodology in reception [24] and found an aperture efficiency above 84% over the entire WR-10 band, in line with the results from [21]. Note that the FO methodology considers the effect of multiple reflections at the lens interface as a loss.

The performance of the single element was then evaluated in terms of its reflection coefficient and radiation patterns in the W-band. These results, along with all results presented from here onwards, are obtained by using full-wave simulations in CST which do include the effects of multiple reflections. The simulated reflection coefficient ( $S_{11}$ ) is shown in Fig. 2(a) (black) and is below -15 dB in the entire bandwidth. The simulated broadside radiation pattern of one of the central embedded elements at 90 GHz is shown in Fig. 2(b)(black). The pattern is nearly rotationally symmetric with sidelobe levels between -17 dB to -20 dB, which is close to the sidelobe level radiated by a uniform circular current distribution, similar to [21]. Thus, the single element is directive enough to achieve a good suppression of the grating lobes in the array factor.

### B. LENS ARRAY PERFORMANCE

We have designed an E-plane linear array, consisting of 4 single lens antenna elements as described in Section II-A, and shown schematically in Fig. 1 (a). The period of the array is

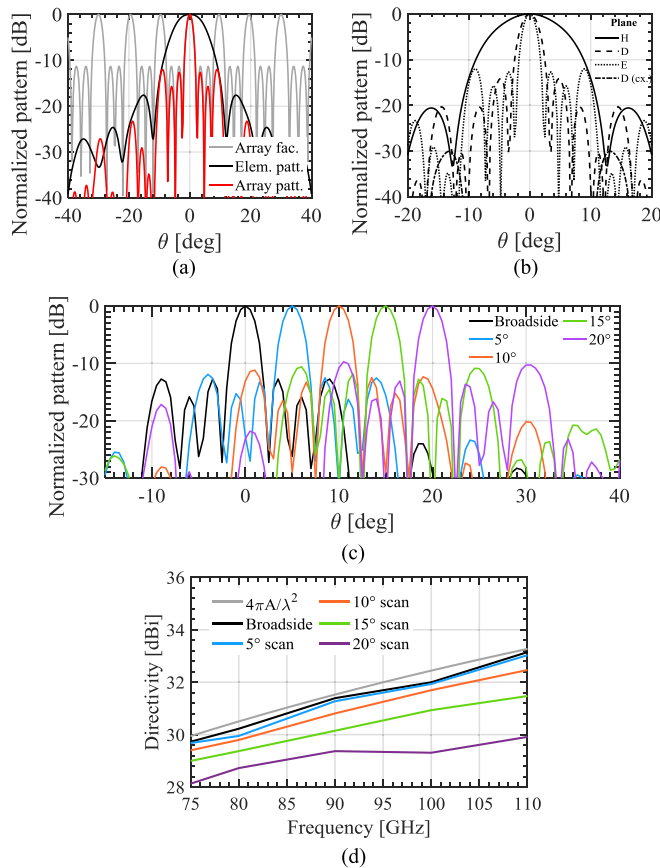


**FIGURE 3.** (a) Simulated array factor, single element pattern and resulting array pattern in the E-plane. (b) Simulated array patterns in the main planes. (c) Simulated E-plane radiation patterns for scanning from broadside up to 20°. All patterns are presented at 90 GHz. (d) Simulated directivity of the 4x1 array in the W-band when scanning towards  $\theta_{sc}$ . The maximum theoretical directivity from an aperture with the array's size is shown for comparison. .

equal to the lens diameter ( $6\lambda_0$ ), which results in the array factor shown in gray in Fig. 3 (a) with grating lobes appearing approximately every  $10^\circ$  in the E-plane. To demonstrate the suppression of the grating lobes, the far-field pattern radiated by the array can be approximated by multiplying the embedded element pattern of Fig. 2 (b) by the array factor. As shown in Fig. 3 (a), the grating lobes are indeed suppressed by the directive single element pattern (black) which results in the array patterns (red). The approximated array pattern obtained in this way is shown in the three main planes in Fig. 3 (b). The resulting array pattern has a sidelobe level below -12 dB (this level can be reduced if the array is designed with a 2D hexagonal grid [7]). Due to the one-dimensionality of the array, the H-plane patterns are equal to the single-element patterns with a maximum sidelobe level of -20 dB. The simulated cross-polarization level of this array is below -40 dB.

To include all the effects of multiple reflections and the effects of the edge elements in the array, we have performed full-wave simulations of the complete array. The broadside

pattern is obtained by in-phase excitation of all elements when the lens array is centered over the elements. For scanned beams, a combination of mechanical displacement of the lens array relative to the feed and progressive phase shifting of each element is applied. For example, the mechanical shift required to scan towards  $\theta_{sc} = 10^\circ$  is 2.4 mm and the progressive phase shift is  $375^\circ$ . The simulated array patterns are shown in Fig. 3(c) at 90 GHz for several scan angles up to  $20^\circ$ . Due to the mechanical displacement, the illumination efficiency of the lens decreases and the sidelobe level of the array pattern increases. Still, the sidelobes are around -10 dB for scan angles up to  $20^\circ$ , which is acceptable for many applications.

The simulated directivity of the complete array is shown as a function of frequency in Fig. 3(d). The achieved directivity is very close to the maximum theoretical directivity of an antenna of such physical dimensions,  $A$ , considered to be four times the area of a single lens. For scan angles up to  $15^\circ$ , the directivity remains within 1.7 dB of the broadside value in the entire W-band. The scan loss of the array is determined by the scan loss of the single element [11].

### C. PROTOTYPE FABRICATION

The designed linear 4x1 array has been fabricated at W-band as shown in Fig. 1(b). The dimensions of the lenses and the corrugations in the ground plane correspond to the simulated dimensions in Section II-A and are indicated in Fig. 1(a). The lens array has been milled from a block of HDPE. The annular corrugations and waveguide array are milled in an aluminum split block. The same fabrication process as [21] was used with comparable fabrication tolerance. Since the design is very wideband, the achieved tolerance does not noticeably impact the performance of the antenna. A photograph of these structures is shown in the inset of Fig. 1(b). The circular waveguides in the top of the ground plane taper to WR-10 waveguide connectors in the bottom of the block.

The circular waveguide is tapered to the WR-10 rectangular waveguide using a linear transition of 17 mm. A piezo-electric motor is connected to the plastic lens array for accurate mechanical displacement of the lens array with respect to the metal block [11], [17]. The speed of the piezo-electric motor is 6 mm/s, resulting in a scan speed of  $25^\circ/\text{s}$  in the current prototype.

### III. EMBEDDED ELEMENT CHARACTERIZATION

In this Section, we present the measured performance of the individual lens elements in the array in terms of  $S_{11}$ , radiation patterns and mutual coupling.

The reflection coefficient of each array element, measured with a VNA and a WR-10 frequency extender, is shown in Fig. 2(a). Due to a fabrication error, the  $b$ -dimension (i.e., the short side of the rectangular waveguide) in the bottom of the split block increased from  $b = 1.26$  mm to  $b = 1.66$  mm. The maximum measured  $S_{11}$  increases from -15 dB for nominal dimensions to -10 dB for the fabricated dimensions. This

result closely matches the simulated  $S_{11}$  with the incorrect waveguide dimensions. Since the circular waveguide at the top of the block has the correct dimensions, the radiation patterns are not affected.

The far-field radiation patterns from each individual array element were calculated from a near-field planar scan measured with a probe 2 cm above the lens. The array element and probe were both connected to a VNA by WR-10 frequency extenders. The measured single-element pattern from one of the lenses is shown in Fig. 2(b) at 90 GHz. The measured patterns are in good agreement with the simulations. However, the cross-polarization is higher at broadside which is attributed to the limited tolerance in the fabrication of the waveguide transition, similar to [21]. In Fig. 4(a) and 4(b), the pattern measurements are shown in the E-plane and H-plane, respectively, for all four individual lens elements at 90 GHz. The measured embedded element patterns are very similar to each other, indicating good manufacturing consistency of the lens array.

The scanned patterns of the embedded element were measured by displacing the lens array relative to the feed with the piezo-electric motor. The simulated and measured E-plane radiation patterns are shown in Fig. 4(c) for scan angles up to  $\theta_{sc} = 20^\circ$  and show good agreement. The mechanical displacement of the piezo-electric motor required to scan the beam is shown in Fig. 4(d) and is  $0.24 \text{ mm}/^\circ$ .

Due to the large period of the array, the mutual coupling between each element is expected to be low. The mutual coupling between each element is simulated to be  $-45 \text{ dB}$  at broadside, which is in good agreement with the measured value as shown in Fig. 4(f). When the lens array is mechanically displaced, the mutual coupling increases. The maximum measured mutual coupling is below  $-30 \text{ dB}$  for the largest mechanical displacement, see Fig. 4(f).

#### IV. ACTIVE ARRAY DEMONSTRATION SETUP

In order to make a demonstration of the dynamic beam steering capabilities of a scanning lens phased array, we developed a setup to achieve electronic control in amplitude and phase of 4 W-band signals, and a setup to calibrate these signals over-the-air.

##### A. ELECTRONIC AMPLITUDE AND PHASE CONTROL SETUP

To simultaneously control the amplitude and phase of the four-element array in the W-band, we use an IQ-steering technique similar to the one described in [20] at Ka-band. A schematic overview of this IQ-steering technique is shown in Fig. 5(a). A continuous-wave  $f_{in} = 12.5 - 18.3 \text{ GHz}$  signal is generated and distributed to four IQ-mixers that individually control the amplitude and phase of their output signal at  $f_{in}$ . The output of these IQ-mixers is fed into 4 frequency extenders that multiply the frequency of the signal by a factor of 6, to end up in the W-band ( $f_{out} = 75 - 110 \text{ GHz}$ ). Since the IQ-mixers can apply a phase shift of  $\phi_{in} = [0, 2\pi]$  to the signal at  $f_{in}$ , the resulting phase shift to the multiplied

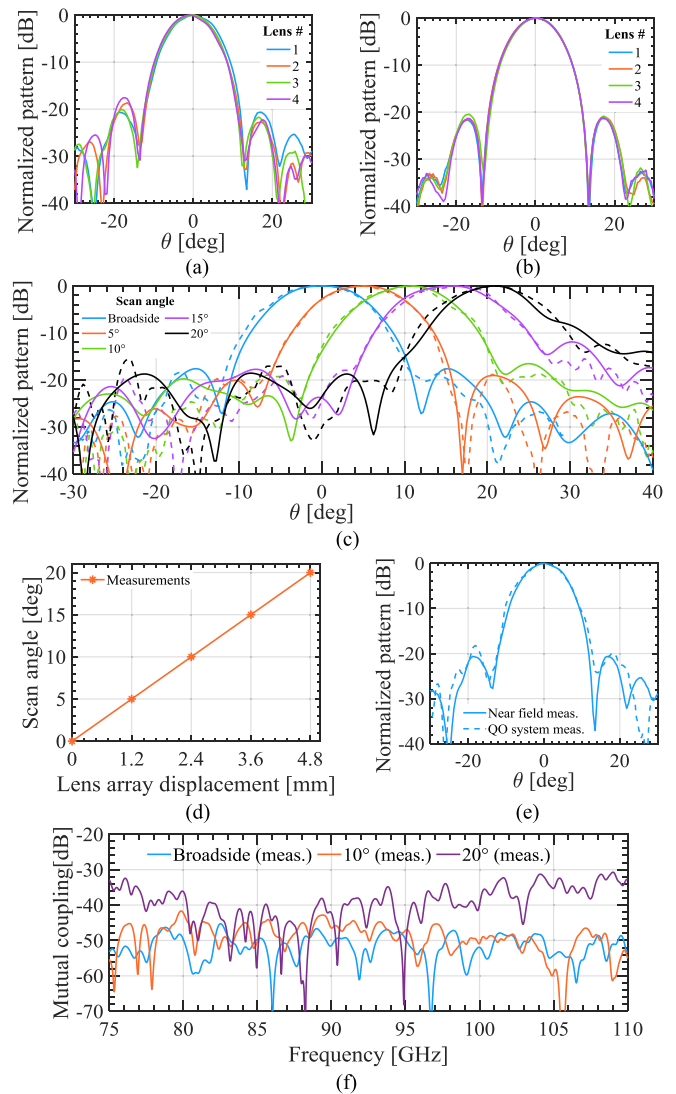


**FIGURE 4.** Measured single-element radiation pattern at 90 GHz of lens elements 1-4 in the (a) E-plane and (b) H-plane and (c) the E-plane when scanning. (d) The required displacement of the lens array with respect to the feed. (e) E-plane pattern measurement: comparison of the near field measurement result and QO measurement result. (f) Measured mutual coupling between two adjacent lenses in the array for several scan positions of the array.

signal is  $\phi_{out} = [0, 12\pi]$ . We thus have four independently controllable channels.

We have implemented the amplitude and phase control architecture of Fig. 5(a) with a signal generator, a four-way Wilkinson power divider, four IQ-mixers, four power amplifiers and four frequency extenders, pictured in Fig. 5(b). Each IQ-mixer is connected to two high-resolution digital-to-analog converters:  $V_I^{(i)}$  and  $V_Q^{(i)}$  with the superscripts ( $i$ ) referring to the channels  $i = 1 \dots 4$  in Fig. 5(a). The voltages  $V_I$ ,  $V_Q$  provide the bias level of the in-phase and quadrature-phase mixer to control the output signals that are summed at the output of the mixer. In this way, the output signal of each IQ-mixer realizes a cartesian vector modulator by varying

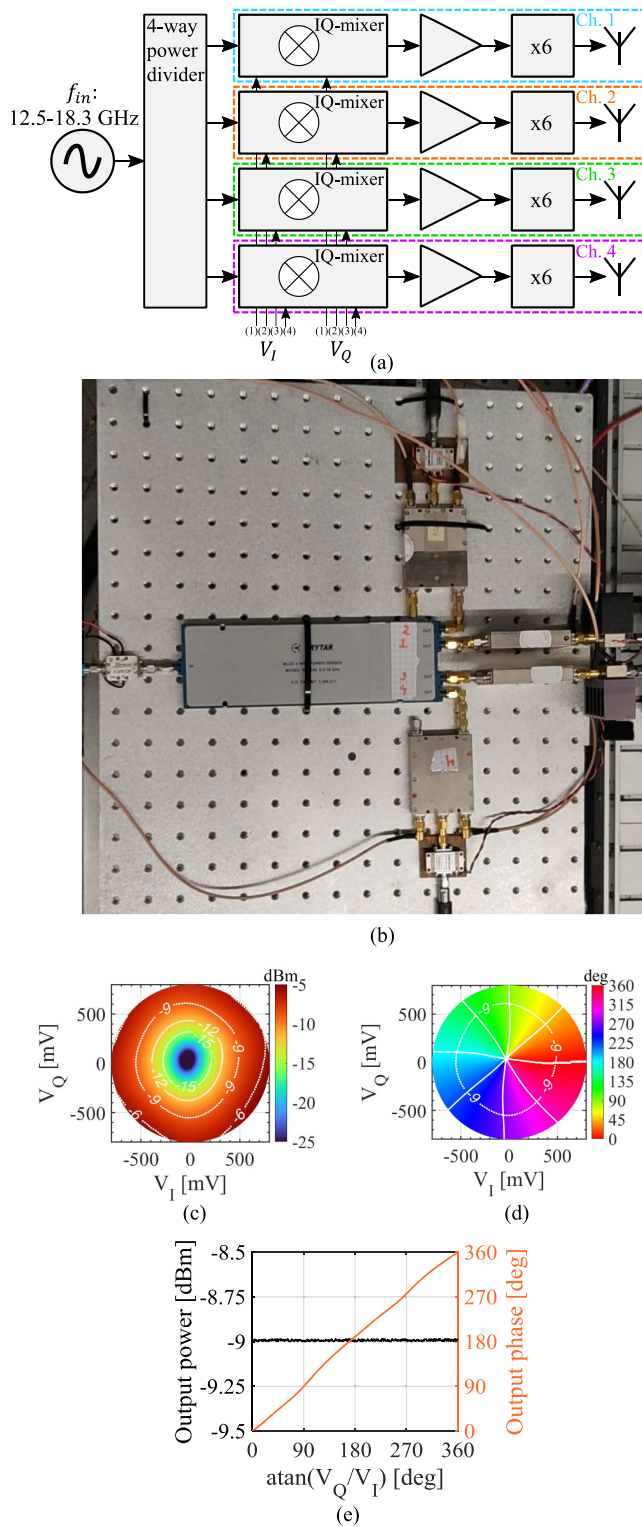


**FIGURE 5.** (a) Schematic of the IQ-steering technique used to control the amplitude and phase fed to the array's elements. (b) Photograph of the implemented IQ-steering electronics. The extenders and antennas are shown in Fig. 6. Measured (c) Power and (d) Relative phase of the IQ-mixer in channel 1 at 15 GHz. Solid lines are constant-phase contours. The -9 dBm power contour is indicated and the measured amplitude and phase on this contour are shown in (e).

the real and imaginary part of the high-frequency signal. In our implementation, the DC voltages are supplied by 12-bit DACs that allow us to control amplitude and phase in steps of  $7 \cdot 10^{-3}$  degrees and  $0.1 \mu W$  at  $f_{in}$ . By implementing the phase shifters at  $f_{in}$  instead of at  $f_{out}$  we are not limited by the performance of W-band phase shifters and we can use commercial components available in our lab to demonstrate the active array. The implementation of the phase shifters represents a significant improvement over earlier lens array demonstrations [4], [18], [19].

The measured output power and phase at 15 GHz, before the frequency extenders, are shown in Fig. 5(c) and (d), respectively. The control of the amplitude will allow us to adjust the input power of each extender in order to achieve the same power level at the output of each frequency extender. The measured output power and relative output phase that corresponds to the -9 dBm contour in Fig. 5(c) and (d) is shown in Fig. 5(e). Indeed, power and phase control are achieved. The IQ-mixers were then connected to the frequency extenders, which were in turn connected to the lens antenna array.

## B. OVER-THE-AIR ACTIVE ARRAY MEASUREMENT SETUP

The far-field distance of the active antenna array (several meters) is larger than our laboratory facilities can accommodate. We have therefore developed a quasi-optical system that will be used to calibrate and measure the active array at a reasonable distance in the lab. The quasi-optical system consists of a focusing lens in front of the array with a focal distance of  $F = 200$  mm. In the region around the focus of this lens, called the spot in the rest of the paper, the field distribution is related to the far field pattern by  $\rho = F \tan \theta$ , where  $\rho$  indicates the lateral distance from lens focus, and  $\theta$  is the far-field radiation angle [25], [26]. Since the field radiated by each array element is coherently summed in the spot, this setup can be used for over-the-air calibration of the channels relative to each other. Furthermore, we can obtain the far-field patterns of the array from a small, planar displacement of the receiver around the spot. The -3 dB spot size is approximately 7.2 mm at 90 GHz and by measuring a  $\pm 170$  mm displacement we can approximately measure the far-field patterns up to  $\pm 40^\circ$ .

To measure the patterns in the spot, only the amplitude must be measured, similar to a far-field measurement setup. We therefore used a WR-10 waveguide probe connected to a commercial down-converting mixer as a receiver, which was connected to a spectrum analyzer for readout of the signals. This receiver provides us with fast measurements of relative power to perform radiation pattern measurements. The measurements with this receiver were later calibrated against absolute power measurements using a power meter, detailed in Section V-B.

A schematic overview of this measurement setup is shown in Fig. 6(a) and photographs of the setup are provided in Fig 6(b) and (c). The amplitude and phase of the array inputs are controlled as described in Section IV-A. The focusing lens

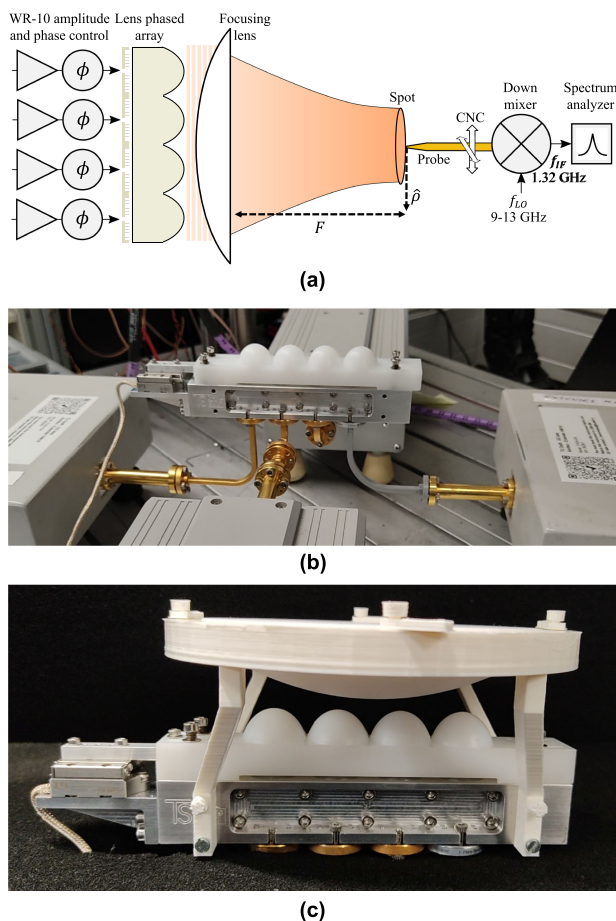


**FIGURE 6.** (a) Schematic of the quasi-optical antenna measurement setup. (b) Frequency extenders connected to the prototype. (c) The PTFE focusing lens is placed above the array.

is a polytetrafluoroethylene (PTFE,  $\epsilon_r = 2$ ) hyperbolic lens placed directly above the antenna array and held in place using a 3-D printed fixture. The receiver is positioned in the spot of the focusing lens and can be moved around it using a 3-axis CNC stage.

To validate the accuracy of the quasi-optical measurement setup, we have compared the measured E-plane pattern of a single active element using this setup to the earlier near-field measurements. Indeed, as shown in Fig. 4(e), there is a good agreement between the two measurement techniques. With this setup we achieve a dynamic range of at least 50 dB. After calibrating the array as described in Section V, the same setup is used to measure the active array patterns.

## V. OVER-THE-AIR ACTIVE ARRAY CALIBRATION

In this section, we describe the calibration procedure necessary for the active array demonstration, that will be presented in Section VI.

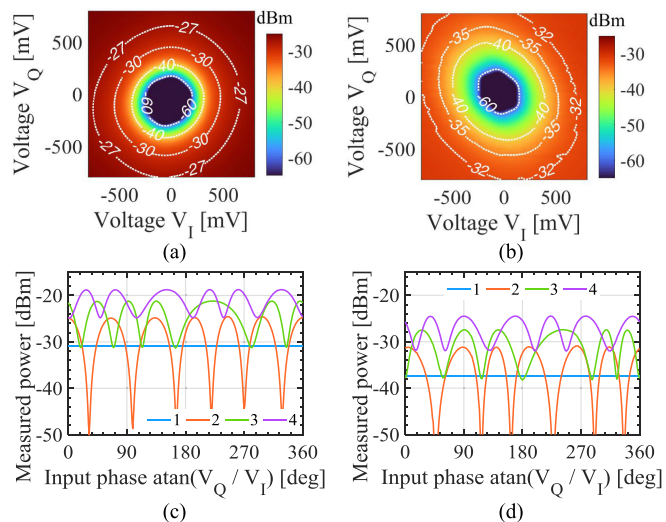


**FIGURE 7.** Received power at 90 GHz for (a) Channel 1 and (b) Channel 2 in the focus of the focusing lens as a function of the IQ-voltages. Received power with 1–4 active channels as a function of  $\phi_{in}$  at (c) 90 GHz, broadside and (d) 102 GHz, 20° scan.

## A. IQ-MIXER CALIBRATION AT W-BAND

The broadside calibration at W-band was performed by positioning the receiver at the focus of the lens and measuring the received power using the spectrum analyzer.

Each lens element of the array was measured independently at 90 GHz as a function of the IQ-mixer voltages  $V_I^{(i)}$ ,  $V_Q^{(i)}$  that control the amplitude and phase fed to the lens. For example, the calibrated measured power at 90 GHz is shown in Fig. 7(a) and (b) for channel 1 and 2, respectively. Due to hardware differences, the received power varies per channel. The greatest common received power for all individual channels, around -31 dBm, was set as the contour in the  $V_I^{(i)}$ ,  $V_Q^{(i)}$ -plane over which each channel operates. A few such constant-power contours are illustrated in Fig. 7(a) and (b).

To demonstrate quasi-optical power combining in the spot, only the first array element is turned on and the power in the spot is measured while the phase angle  $\phi_{in}^{(1)} = \text{atan}(V_Q^{(1)}/V_I^{(1)})$  is swept from  $0^\circ$  to  $360^\circ$  over the contour of constant power. The calibrated measured power is shown in Fig. 7(c), where we see that indeed -31 dBm is measured independent of  $\phi_{in}^{(1)}$ . The first array element is then fixed at  $\phi_{in}^{(1)} = 0^\circ$  and the second array element is turned on. We then measure the received power, i.e., the combined power of channels 1 and 2, as a function of the phase angle  $\phi_{in}^{(2)} = [0^\circ, 360^\circ]$  over its contour of equal power. A clear interference pattern with 6 constructive (destructive) peaks (valleys) can be observed in the measured power in Fig. 7(c), which is consistent with the phase shifting after the frequency extenders achieving a range of  $[0, 12\pi]$ .

For the channels  $i = \{3, 4\}$ , the preceding steps are repeated: channels  $1 \dots i - 1$  are fixed at a point of maximum constructive interference. Channel  $i$  is turned on and  $\phi_{in}^{(i)}$  is swept over a contour of constant power. The measured power

**TABLE 1. Measured Power in the Measurement Setup**

Frequency [GHz]	$P_{spot}^{SA}$ [dBm] at $f_{IF}$	$P_{spot}^{PM}$ [dBm] at $f_{out}$	$P_{in}^{PM}$ [dBm] at $f_{out}$
78	-44.4	-16.7	0.6
90	-45.2	-18.6	-2.9
102	-57.0	-21.2	-6.0

is shown in Fig. 7(c), in which the characteristic peaks and valleys are indeed observed. The maximum received power with four active lens elements is 12 dB above the received power of a single antenna element, as expected from the increased antenna gain and transmit power. Maximum destructive interference with four active channels is 6 dB below the maximum constructive interference, which is expected since channels 1-3 are fed in phase and only the fourth channel is out of phase.

The calibration procedure for scanned beams is the same as the procedure outlined above, except for the position of the piezo-electric motor and the position of the receiver. The piezo-electric motor was displaced by 0.24 mm per degree of desired scan angle (see Section III). The receiver was positioned at the scanned focus of the focusing lens which is displaced  $\Delta\rho = F \tan(\theta_{sc})$  relative to the broadside spot of the focusing lens.

The calibration procedure described above was performed for 78 GHz, 90 GHz and 102 GHz for scan angles up to  $\theta_{sc} = 20^\circ$  in steps of  $\Delta\theta_{sc} = 5^\circ$ . For example, the received power with 1-4 active channels as a function of  $\phi_{in}^{(i)}$  for  $\theta_{sc} = 20^\circ$  at 102 GHz is shown in Fig. 7(d) where we can also observe the 12 dB gain in received power of the active array relative to a single active element. This calibration procedure provides us with the values for the IQ-mixer voltages  $V_I^{(i)}$ ,  $V_Q^{(i)}$  that correspond to the progressive phase shifts required to steer the beam towards the desired scan angle  $\theta_{sc}$ .

### B. ABSOLUTE POWER CALIBRATION

After calibration, we measured the power in the spot radiated by the active array using a standard gain horn and a W-band power meter. The measured power was used to calibrate the relative power measurements performed with the spectrum analyzer. The measured power in the spot with both setups is reported in Table 1 as  $P_{spot}^{SA}$  (spectrum analyzer) and  $P_{spot}^{PM}$  (power meter), respectively. Finally, the input power to the array,  $P_{in}^{PM}$ , was measured by summing the power measured at the output of the frequency extenders with a power meter. This power is also reported in Table 1.

### VI. ACTIVE ARRAY DEMONSTRATION

The active 4x1 scanning lens phased array performance was measured using the setup and calibration procedure described in Sections IV and V.

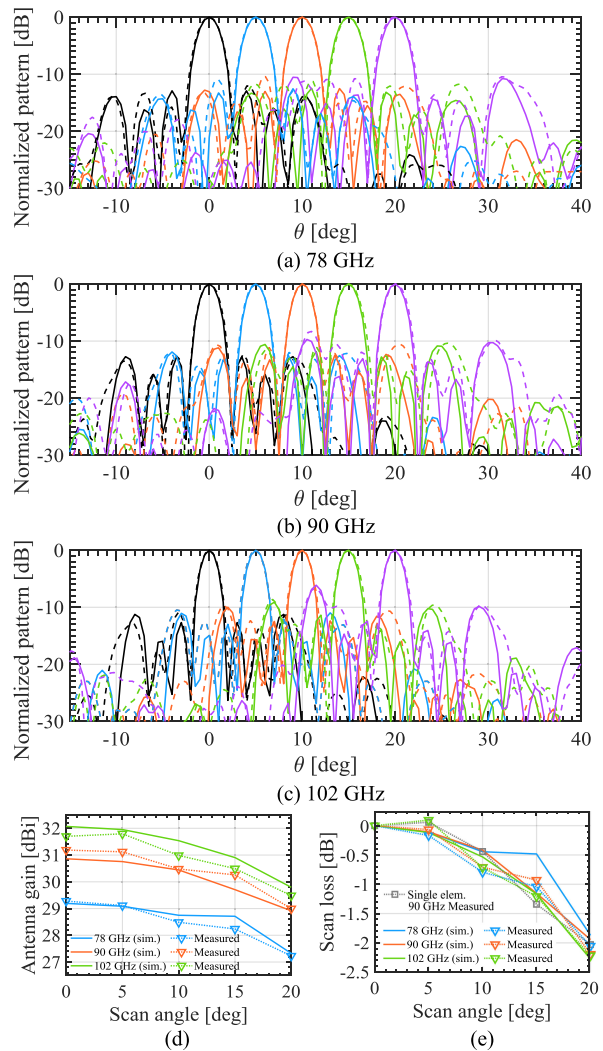


**FIGURE 8. (a)-(c) 4x1 active array E-plane radiation patterns at 78-102 GHz. The achieved (d) Antenna gain and (e) Scan loss of the active array. Solid lines are simulations, dashes are measurements.**

The measured broadside E-plane radiation patterns of the active array are shown in Fig. 8(a)-(c) at 78 GHz, 90 GHz and 102 GHz, respectively. The radiation patterns show excellent agreement with full-wave array simulations of the far field patterns for all frequencies. The maximum sidelobe level is around  $-12$  dB in the E-plane and around  $-20$  dB in the H-plane.

The measured scanned E-plane radiation patterns are shown in Fig. 8(a)-(c) at 78 GHz, 90 GHz and 102 GHz, respectively. The scanned patterns also show very good agreement with the expected patterns from the simulations, with maximum sidelobe level increasing to around  $-10$  dB for  $\theta_{sc} = 15^\circ$ .

The array's antenna gain is obtained by applying Friis' equation, which can still be applied in the focused spot as explained in [26]. The transmit power is  $P_{in}^{PM}$ , the received power is  $P_{spot}^{PM}$  as reported in Section V-B and Table 1. The gain of the horn is 10.8 dBi at 90 GHz. The dielectric and reflection

loss due to the PTFE focusing lens is estimated at 0.36 dB ( $\tan \delta = 4 \cdot 10^{-4}$  [27]). The measured antenna gain is shown in Fig. 8(d) for 78-102 GHz. For broadside, the measured gain is 31.2 dBi at 90 GHz. The simulated gain in Fig. 8(d) takes into account the estimated dielectric loss in the lens array of 0.07 dB ( $\tan \delta = 3.3 \cdot 10^{-4}$  [27]) and the ohmic loss in the waveguide block between 0.5-0.75 dB ( $\sigma = 3.6 \cdot 10^5$  S/m [21]).

The measured scan loss is determined as the difference in received power in a scanned position relative to broadside, taking the pattern of the receiving probe in consideration, and is shown in Fig. 8(e). The measured scan loss is in good agreement with the simulated scan loss and is between -2 dB and -2.2 dB for  $\theta_{sc} = 20^\circ$  in the W-band, depending on the frequency. The measured scan loss of a single element is also shown in Fig. 8(e), demonstrating that the scan loss is indeed defined by the scanning ability of the single element as anticipated in [11]. Consequently, the scan loss of the array and grating lobe levels can be improved by using lens elements with better scanning performance. The antenna gain as a function of scan angle, shown in Fig. 8(d), is in good agreement with simulations.

Although other works at lower frequencies, such as [18] and [19], have demonstrated beam scanning to larger angles, i.e.,  $\theta_{sc} = 30^\circ$ , the gain reported in those works was much lower: below 20 dBi for roughly the same number of array elements. This is due to the smaller diameter of the single lenses:  $D_l \approx 2.5\lambda_0$  in [18] and [19] versus  $D_l = 6\lambda_0$  in this work. Consequently, the maximum number of beams scanned  $N = \theta_{sc}D_l/\lambda_0$  is  $N \approx 1.3$  in [18], [19] and  $N = 2.1$  in this work. Scanning  $N = 1.3$  beams ( $\theta_{sc} = 12.5^\circ$ ) using our antenna results in a scan loss of around 0.9 dB, which is lower than the 1.6 dB and 2.5 dB scan loss reported in [18] and [19], respectively, for the same  $N$ . Additionally, the pattern quality and aperture efficiency in [18] and [19] are not as high as reported here. For example, in [18] the aperture efficiency is below 40% while we achieve around 84%. In [19] the sidelobe level is around -6 dB for  $N = 1$  while we remain below -10 dB for  $N = 2$ . Finally, the measured bandwidth of our antenna is more than 25%, while the bandwidths in [18] and [19] are 11% and 8.5%, respectively.

## VII. CONCLUSION

We have reported on the simulation, fabrication and measurement of a sparse 4x1 scanning lens phased array with a periodicity of  $6\lambda_0$  operating over the entire W-band (75-110 GHz). The array is capable of continuous and dynamic beam steering of a high-gain (>30 dBi) beam towards  $\pm 20^\circ$  with low grating lobe levels around -10 dB. The array achieves low grating lobe level thanks to the use of a leaky wave feed in combination with HDPE lenses to reach high aperture efficiency illumination of the lens that is required in the scanning lens phased array architecture.

The active scanning lens phased array relies on a combination of electrical and mechanical phase shifting to steer the

beams. To achieve electrical phase shifting, we developed and measured a W-band setup that uses IQ-mixers at low frequencies to achieve  $[0, 2\pi]$  phase shift before x6 multiplication, resulting in  $[0, 12\pi]$  phase control at W-band. Mechanical phase shifting was implemented with a high-precision piezoelectric motor. The proposed dynamic beam steering concept can be extended to two dimensions using 2-D piezo-electric motors. This will enable translating the lens array in the  $xy$ -plane, achieving the steering of the element pattern in two dimensions.

An over-the-air active array calibration method was presented and implemented. Measurements of this W-band 4x1 array prototype show excellent agreement with simulations in terms of radiation patterns, gain and scan performance, demonstrating the potential of the proposed scanning lens phased array concept.

## ACKNOWLEDGMENT

We thank the Microwave Sensing, Signals and Systems group at Delft University of Technology for kindly lending us two frequency extenders for this demonstration.

## REFERENCES

- [1] T. S. Rappaport *et al.*, "Wireless communications and applications above 100 GHz: Opportunities and challenges for 6G and beyond," *IEEE Access*, vol. 7, pp. 78729–78757, 2019, doi: [10.1109/ACCESS.2019.2921522](https://doi.org/10.1109/ACCESS.2019.2921522).
- [2] X. Gu, A. Valdes-Garcia, A. Natarajan, B. Sadhu, D. Liu, and S. K. Reynolds, "W-band scalable phased arrays for imaging and communications," *IEEE Commun. Mag.*, vol. 53, no. 4, pp. 196–204, Apr. 2015, doi: [10.1109/MCOM.2015.7081095](https://doi.org/10.1109/MCOM.2015.7081095).
- [3] J. Edstam, J. Hansryd, S. Carpenter, T. Emanuelsson, Y. Li, and H. Zirath, *Microwave Backhaul Evolution – Reaching Beyond 100GHz*. Stockholm, Sweden: Ericsson Technology Review, 2017.
- [4] H. Zhang, S. Bosma, A. Neto, and N. Llombart, "A dual-polarized 27dBi scanning lens phased array antenna for 5G point-to-point communications," *IEEE Trans. Antennas Propag.*, vol. 69, no. 9, pp. 5640–5652, Sep. 2021, doi: [10.1109/TAP.2021.3069494](https://doi.org/10.1109/TAP.2021.3069494).
- [5] W. Lee *et al.*, "Fully integrated 94-GHz dual-polarized TX and RX phased array chipset in SiGe BiCMOS operating up to 105 °C," *IEEE J. Solid-State Circuits*, vol. 53, no. 9, pp. 2512–2531, Sep. 2018, doi: [10.1109/JSSC.2018.2856254](https://doi.org/10.1109/JSSC.2018.2856254).
- [6] W. Shin, B.-H. Ku, O. Inac, Y.-C. Ou, and G. M. Rebeiz, "A 108–114 GHz  $4 \times 4$  wafer-scale phased array transmitter with high-efficiency on-chip antennas," *IEEE J. Solid-State Circuits*, vol. 48, no. 9, pp. 2041–2055, Sep. 2013, doi: [10.1109/JSSC.2013.2260097](https://doi.org/10.1109/JSSC.2013.2260097).
- [7] S. Shahramian, M. J. Holyoak, and Y. Baeyens, "A 16-element W-band phased-array transceiver chipset with flip-chip PCB integrated antennas for multi-gigabit wireless data links," *IEEE Trans. Microw. Theory Techn.*, vol. 66, no. 7, pp. 3389–3402, Jul. 2018, doi: [10.1109/TMTT.2018.2822304](https://doi.org/10.1109/TMTT.2018.2822304).
- [8] S. Li, Z. Zhang, B. Rupakula, and G. M. Rebeiz, "An eight-element 140-GHz wafer-scale IF beamforming phased-array receiver with 64-QAM operation in CMOS RFSOI," *IEEE J. Solid-State Circuits*, vol. 57, no. 2, pp. 385–399, Feb. 2022, doi: [10.1109/JSSC.2021.3102876](https://doi.org/10.1109/JSSC.2021.3102876).
- [9] S. Kang, S. V. Thyagarajan, and A. M. Niknejad, "A 240 GHz fully integrated wideband QPSK transmitter in 65 nm CMOS," *IEEE J. Solid-State Circuits*, vol. 50, no. 10, pp. 2256–2267, Oct. 2015, doi: [10.1109/JSSC.2015.2467179](https://doi.org/10.1109/JSSC.2015.2467179).
- [10] K. Guo, Y. Zhang, and P. Reynaert, "A 0.53-THz subharmonic injection-locked phased array with 63- $\mu$  W radiated power in 40-nm CMOS," *IEEE J. Solid-State Circuits*, vol. 54, no. 2, pp. 380–391, Feb. 2019, doi: [10.1109/JSSC.2018.2877203](https://doi.org/10.1109/JSSC.2018.2877203).



- [11] M. Alonso-delPino, S. Bosma, C. Jung-Kubiak, G. Chattopadhyay, and N. Llombart, "Wideband multimode leaky-wave feed for scanning lens-phased array at submillimeter wavelengths," *IEEE Trans. THz Sci. Technol.*, vol. 11, no. 2, pp. 205–217, Mar. 2021, doi: [10.1109/TTHZ.2020.3038033](https://doi.org/10.1109/TTHZ.2020.3038033).
- [12] R. Mailloux, L. Zahn, and A. Martinez, "Grating lobe control in limited scan arrays," *IEEE Trans. Antennas Propag.*, vol. 27, no. 1, pp. 79–85, Jan. 1979, doi: [10.1109/TAP.1979.1142034](https://doi.org/10.1109/TAP.1979.1142034).
- [13] F. Scattone, M. Ettore, B. Fuchs, R. Sauleau, and N. J. G. Fonseca, "Synthesis procedure for thinned leaky-wave-based arrays with reduced number of elements," *IEEE Trans. Antennas Propag.*, vol. 64, no. 2, pp. 582–590, Feb. 2016, doi: [10.1109/TAP.2015.2509008](https://doi.org/10.1109/TAP.2015.2509008).
- [14] D. Blanco, N. Llombart, and E. Rajo-Iglesias, "On the use of leaky wave phased arrays for the reduction of the grating lobe level," *IEEE Trans. Antennas Propag.*, vol. 62, no. 4, pp. 1789–1795, Apr. 2014, doi: [10.1109/TAP.2013.2272573](https://doi.org/10.1109/TAP.2013.2272573).
- [15] B. Avser, J. Pierro, and G. M. Rebeiz, "Random feeding networks for reducing the number of phase shifters in limited-scan arrays," *IEEE Trans. Antennas Propag.*, vol. 64, no. 11, pp. 4648–4658, Nov. 2016, doi: [10.1109/TAP.2016.2600861](https://doi.org/10.1109/TAP.2016.2600861).
- [16] D. Petrolati, P. Angeletti, and G. Toso, "A lossless beam-forming network for linear arrays based on overlapped sub-arrays," *IEEE Trans. Antennas Propag.*, vol. 62, no. 4, pp. 1769–1778, Apr. 2014, doi: [10.1109/TAP.2013.2282189](https://doi.org/10.1109/TAP.2013.2282189).
- [17] M. Alonso-delPino, C. Jung-Kubiak, T. Reck, N. Llombart, and G. Chattopadhyay, "Beam scanning of silicon lens antennas using integrated piezomotors at submillimeter wavelengths," *IEEE Trans. THz Sci. Technol.*, vol. 9, no. 1, pp. 47–54, Jan. 2019, doi: [10.1109/TTHZ.2018.2881930](https://doi.org/10.1109/TTHZ.2018.2881930).
- [18] R. Xu and Z. N. Chen, "A compact beamsteering metasurface lens array antenna with low-cost phased array," *IEEE Trans. Antennas Propag.*, vol. 69, no. 4, pp. 1992–2002, Apr. 2021, doi: [10.1109/TAP.2020.3026905](https://doi.org/10.1109/TAP.2020.3026905).
- [19] G. Mumcu, M. Kacar, and J. Mendoza, "Mm-wave beam steering antenna with reduced hardware complexity using lens antenna subarrays," *IEEE Antennas Wireless Propag. Lett.*, vol. 17, no. 9, pp. 1603–1607, Sep. 2018, doi: [10.1109/LAWP.2018.2857441](https://doi.org/10.1109/LAWP.2018.2857441).
- [20] A. Visweswaran, C. de Martino, E. Sirignano, and M. Spirito, "An IQ-steering technique for amplitude and phase control of mm-wave signals," in *Proc. 86th ARFTG Microw. Meas. Conf.*, 2015, pp. 1–4, doi: [10.1109/ARFTG.2015.7381471](https://doi.org/10.1109/ARFTG.2015.7381471).
- [21] S. Bosma, N. van Rooijen, M. Alonso-delPino, and N. Llombart, "A wideband leaky-wave lens antenna with annular corrugations in the ground plane," *IEEE Antennas Wireless Propag. Lett.*, early access, May 23, 2022, doi: [10.1109/LAWP.2022.3176884](https://doi.org/10.1109/LAWP.2022.3176884).
- [22] N. Llombart, G. Chattopadhyay, A. Skalare, and I. Mehdi, "Novel terahertz antenna based on a silicon lens fed by a leaky wave enhanced waveguide," *IEEE Trans. Antennas Propag.*, vol. 59, no. 6, pp. 2160–2168, Jun. 2011, doi: [10.1109/TAP.2011.2143663](https://doi.org/10.1109/TAP.2011.2143663).
- [23] S. Bosma, A. Neto, and N. Llombart, "On the near-field spherical wave formation in resonant leaky-wave antennas: Application to small lens design," *IEEE Trans. Antennas Propag.*, vol. 70, no. 2, pp. 801–812, Feb. 2022, doi: [10.1109/TAP.2021.3137238](https://doi.org/10.1109/TAP.2021.3137238).
- [24] H. Zhang, S. O. Dabironezare, G. Carluccio, A. Neto, and N. Llombart, "A Fourier optics tool to derive the plane wave spectrum of quasi-optical systems [EM programmer's notebook]," *IEEE Antennas Propag. Mag.*, vol. 63, no. 1, pp. 103–116, Feb. 2021, doi: [10.1109/MAP.2020.3027233](https://doi.org/10.1109/MAP.2020.3027233).
- [25] S. van Berkel *et al.*, "Wideband double leaky slot lens antennas in CMOS technology at submillimeter wavelengths," *IEEE Trans. THz Sci. Technol.*, vol. 10, no. 5, pp. 540–553, Sep. 2020, doi: [10.1109/TTHZ.2020.3006750](https://doi.org/10.1109/TTHZ.2020.3006750).
- [26] E. Gandini, A. Tamminen, A. Luukanen, and N. Llombart, "Wide field of view inversely magnified dual-lens for near-field submillimeter wavelength imagers," *IEEE Trans. Antennas Propag.*, vol. 66, no. 2, pp. 541–549, Feb. 2018, doi: [10.1109/TAP.2017.2778016](https://doi.org/10.1109/TAP.2017.2778016).
- [27] J. W. Lamb, "Miscellaneous data on materials for millimetre and sub-millimetre optics," *Int. J. Infrared Millimeter Waves*, vol. 17, no. 12, pp. 1997–2034, Dec. 1996, doi: [10.1007/BF02069487](https://doi.org/10.1007/BF02069487).



(sub)millimeter-waves.

**SJOERD BOSMA** (Graduate Student Member, IEEE) received the B.Sc. degree and the M.Sc. degree (*cum laude*) in electrical engineering from the Delft University of Technology (TU Delft), Delft, The Netherlands, in 2015 and 2017, respectively. He is currently working toward the Ph.D. degree with Terahertz Sensing Group, TU Delft. From September 2018 to February 2019, he participated in the JPL Visiting Student Researcher Program at Jet Propulsion Laboratory, Pasadena, CA, USA. He is working on leaky-wave lens antenna arrays at



analysis, design, and measurement of integrated lens antennas and leaky-wave structures.

Mr. Van Rooijen was the co-recipient of the Best Theory And Design Antenna Paper Award and was also nominated for the Best Applied Technology Antenna Paper Award, both at the 16th European Conference on Antennas and Propagation (EuCAP) in 2022.

**NICK VAN ROOIJEN** received the M.Sc. degree (*cum laude*) in electrical engineering from the Delft University of Technology (TU Delft), Delft, The Netherlands, in 2021, where he is currently working toward the Ph.D. degree with Terahertz Sensing Group. At TU Delft, his research focuses on the development of a Fly's eye lens array for high frequency communication applications. During the master's, he worked on a first-time demonstration of a high frequency scanning-lens phased-array. His research interests include the



(TU Delft), Delft, The Netherlands. From 2015 to 2016, she was a NASA Postdoctoral Fellow with Jet Propulsion Laboratory (JPL), Pasadena, CA, USA. From 2016 to 2020, she was a Member of the Technical Staff with the Sub-millimeter Wave Advanced Technology Group of JPL/NASA. Since 2020, she has been an Assistant Professor with TU Delft. Her research interests include millimeter and submillimeter-wave heterodyne and direct detection receiver technologies, antennas, and quasi-optical systems.

Dr. Alonso-Delpino was the recipient of the Outstanding Reviewer Award of the IEEE Transactions on Terahertz Science and Technology in 2013 and a co-recipient of the 2014 IEEE Terahertz Science and Technology Best Paper Award.

**MARIA ALONSO-DELPINO** (Senior Member, IEEE) received the Degree in telecommunications engineering from the Technical University of Catalonia (UPC), Barcelona, Spain, in 2008, the M.S. degree in electrical engineering from the Illinois Institute of Technology, Chicago, IL, USA, in 2008, and the Ph.D. degree in signal theory and communications/electrical engineering from UPC in 2013.



**MARCO SPIRITO** (Member, IEEE) received the M.Sc. degree (*cum laude*) in electrical engineering from the University of Naples Federico II, Naples, Italy, in 2000, and the Ph.D. degree in microelectronics from the Delft University of Technology, Delft, The Netherlands, in 2006.

From 2000 to 2001, he was a Guest Researcher with Infineon Technologies, Munich, Germany. In 2006, he joined the Department of Electronics and Telecommunications Engineering, University of Naples Federico II. In April 2008, he was an As-

stant Professor with the Electronics Research Laboratory, Delft University of Technology, where he has been an Associate Professor since April 2013. In 2010 and 2017, he was one of the co-founders of Anteverta-MW, Eindhoven, The Netherlands, and Vertigo Technologies, Delft, respectively, two companies pioneering innovative measurement techniques and instruments. His research interests include the development of advanced passive components and building blocks operating in the millimeter and submillimeter frequency ranges, development of characterization setups and calibration techniques for millimeter and submillimeter waves, and design and integration of millimeter-wave sensing systems.

Dr. Spirito was the recipient of the Best Student Paper Award for his contribution to the 2002 IEEE Bipolar/BiCMOS Circuits and Technology Meeting. He was the recipient of the IEEE Microwave Theory and Techniques Society Microwave Prize in 2008. He was a co-recipient of the Best Student Paper Award at the 2011 IEEE Radio Frequency Integrated Circuits Symposium, GAAS Association Student Fellowship in 2012, Best Student Paper Award in second place at the 2018 International Microwave Biomedical Conference, Best Paper Award at the 2019 Winter ARFTG Conference, and Best Student Paper Award at the 2019 Summer ARFTG Conference.



**NURIA LLOMBART** (Fellow, IEEE) received the master's degree in electrical engineering and Ph.D. degree from the Polytechnic University of Valencia, Valencia, Spain, in 2002 and 2006, respectively.

During the master's degree studies, she spent one year with the Friedrich Alexander University of Erlangen Nuremberg, Erlangen, Germany, and with the Fraunhofer Institute for Integrated Circuits, Erlangen. From 2002 to 2007, she was with Antenna Group, TNO Defense, Security and Safety

Institute, The Hague, The Netherlands, working as a Ph.D. Student and then as a Researcher. From 2007 to 2010, she was a Postdoctoral Fellow with the California Institute of Technology, Submillimeter Wave Advance Technology Group, Jet Propulsion Laboratory, Pasadena, CA, USA. From 2010 to 2012, she was a Ramón y Cajal Fellow with the Optics Department, Complutense University of Madrid, Madrid, Spain. In September 2012, she joined the THz Sensing Group, Technical University of Delft, Delft, The Netherlands, where she has been a Full Professor since February 2018. She has coauthored more than 150 journal and international conference contributions. Her research interests include the analysis and design of planar antennas, periodic structures, reflector antennas, lens antennas, and waveguide structures, with emphasis in the THz range.

Dr. Llombart was the recipient H. A. Wheeler Award for the Best Applications Paper of 2008 in IEEE TRANSACTIONS ON ANTENNAS AND PROPAGATION, 2014 THz Science and Technology Best Paper Award of the IEEE Microwave Theory and Techniques Society, and several NASA awards. She was also the recipient of the 2014 IEEE Antenna and Propagation Society Lot Shafai Mid-Career Distinguished Achievement Award. She is a Board member of the IRMMW-THz International Society. In 2015, she was the recipient of a European Research Council Starting Grant. She was the co-recipient of the Best Theory and Antenna Design Paper Award at the 16th European Conference on Antennas and Propagation (EuCAP), 2022. In 2019, she became IEEE Fellow for contributions to millimeter and submillimeter-wave quasi-optical systems.